Oxygen vacancies confined $CoMoO_4$@$CoNiO_2$ nanorod arrays for oxygen evolution with improved performance

Xiaoqiang Du[a*], Guangyu Ma, [a] and Xiaoshuang Zhang,[b*]

a. School of Chemical Engineering and Technology, North University of China, Taiyuan 030051, People's Republic of China. E-mail: duxq16@nuc.edu.cn

b. School of Science, North University of China, E-mail: 20160068@nuc.edu.cn

Experimental section

Characterization of materials

The purity and composition of the catalyst are characterized by X-ray powder diffraction (XRD) using an Empyrean. The morphology of the catalyst is characterized by a HITACHI SU8020 Scanning electron microscopy (SEM) images, and the surface properties and valence states of the catalyst are characterized by X-ray photoelectron spectra (XPS) measurements.

Electrochemical measurement

Electrochemical measurements were made using a classical three-electrode system with platinum wire (OER) or graphite electrode (HER) as the counter electrode, Ag/AgCl as reference electrode and the resulting material as the working electrode. Chronoamperometric was acted to a method to study their stability for OER and HER. The faradic efficiency (FE) was calculated as the ratio between the quantity of oxygen or hydrogen production for theoretical and experimental.

DFT computation details: The DFT calculations were performed using the Cambridge Sequential Total Energy Package (CASTEP) with the plane-wave pseudo-potential method. The geometrical structures of the (111) plane of $NiCoO_2$ were optimized by the generalized gradient approximation (GGA) methods. The Revised Perdew-Burke-Ernzerh of (RPBE) functional was used to treat the electron exchange correlation interactions. A Monkhorst Pack grid k-points of $3\times3\times2$ and a plane-wave basis set cut-off energy of 400 eV were used for integration of the Brillouin zone. The structures were optimized for energy and force convergence set at 0.03 eV/A and 1.0×10^{-5} eV, respectively. A self-consistence field of 2.0×10^{-6} eV/atom was applied. A vacuum space as large as 15.0 A was used to avoid periodic interactions. The free energy ($\triangle G_{H^*}$) for hydrogen absorption was computed as;

$$\triangle G_{H^*} = E_{total} + E_{surf} - 1/2E_{H2} + \triangle ZPE - T\triangle S$$

The symbols represent the total energy (E_{total}) for adsorbed state, energy of pure state (E_{surf}), the change in zero-point energy ($\triangle E_{ZPE}$), Temperature (T), and the entropy change ($\triangle S$), respectively. It is estimated that the vibrational entropy of hydrogen in the adsorbed state is negligible such that $\triangle S_H \approx \triangle_{H^*} - 1/2(S_{H2}) \approx -1/2(S_{H2})$, where S_{H2} is the entropy of $H_{2(g)}$ at standard conditions and $TS_{(H2)}$ is given as about 0.41 eV for H_2 at 300 K and 1 atm.

Theoretical models: The correlative models are constructed to simulate $CoMoO_4$@$CoNiO_2$/O_2 and composite $CoMoO_4$@$CoNiO_2$/Ar catalyst. Typically, the (111) facet of $CoNiO_2$ was modeled by the slab with layers of Ni-O atoms terminated by H-atoms, and the (111) facet was adopted to create the $CoNiO_2$ slab.

N_2 adsorption for Brunauer–Emmett–Teller (BET) surface area determination: Nitrogen adsorption/desorption at T=77K was performed with a Micromeritics ASAP 2020M system. Sample was used for adsorption analysis after pretreatment at T=80°C for t=8.0h under vacuum conditions and the sample was kept in an N_2 atmosphere until N_2-adsorption measurements were performed. Surface areas were calculated from the adsorption data by using Langmuir and BET

methods

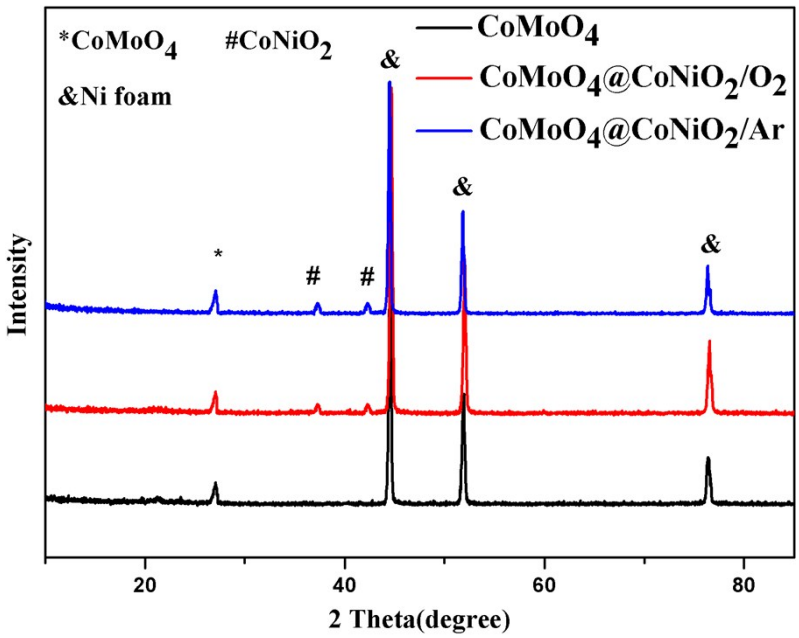

Fig. S1 XRD of $CoMoO_4$, $CoMoO_4$@$CoNiO_2$/O_2 and $CoMoO_4$@$CoNiO_2$/Ar.

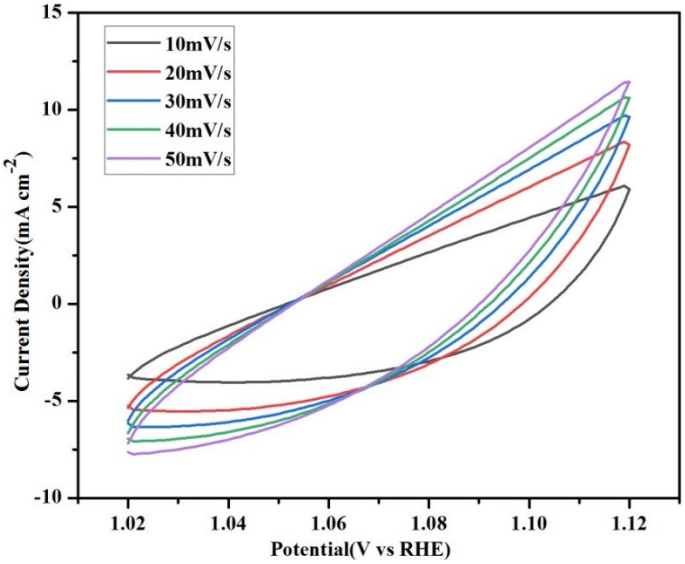

Fig. S2 CV_S of $CoMoO_4$ with different scan rates (10-50 mV s^{-1}) in the region of 1.02-1.12V *vs* RHE.

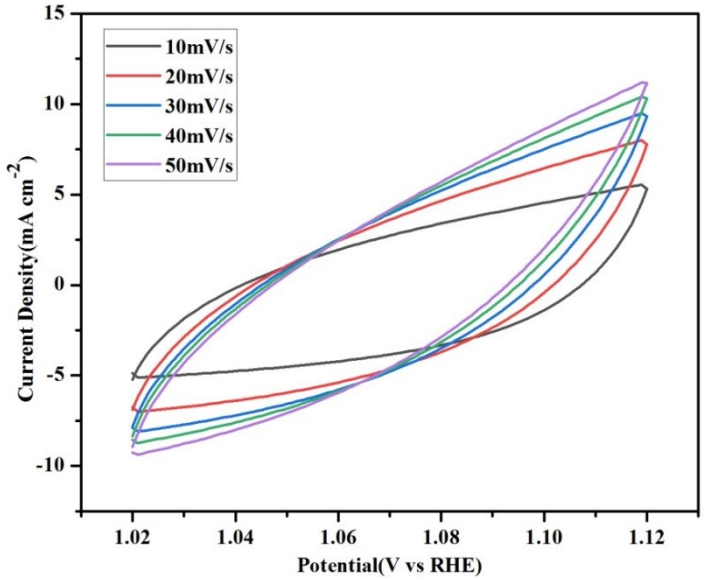

Fig. S3 CV_S of $CoMoO_4$@$CoNiO_2$/O_2 with different scan rates (10-50 mV s^{-1}) in the region of 1.02-1.12V *vs* RHE.

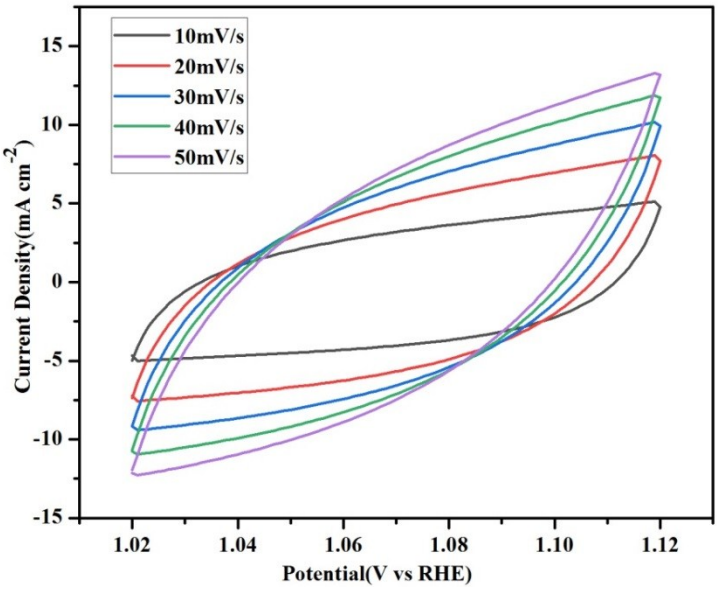

Fig. S4 CV_S of $CoMoO_4$@$CoNiO_2$/Ar with different scan rates (10-50 mV s^{-1}) in the region of 1.02-1.12V *vs* RHE.

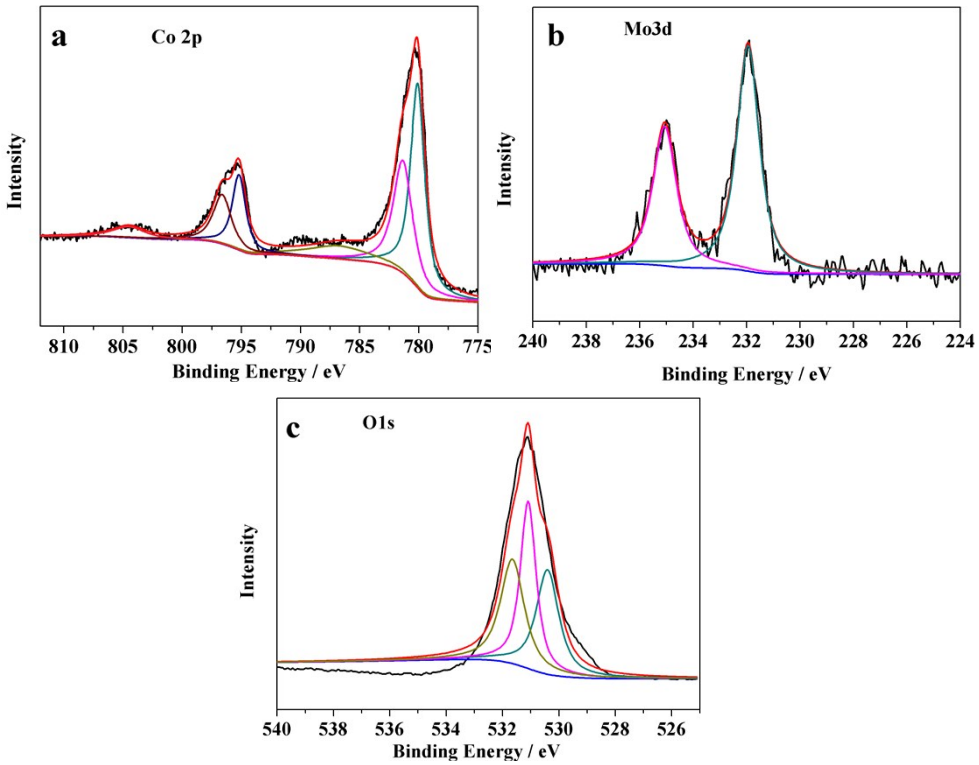

Fig.S5 XPS of (a) Co 2p, (b) Mo 3d and (c) O 1s of $CoMoO_4$.

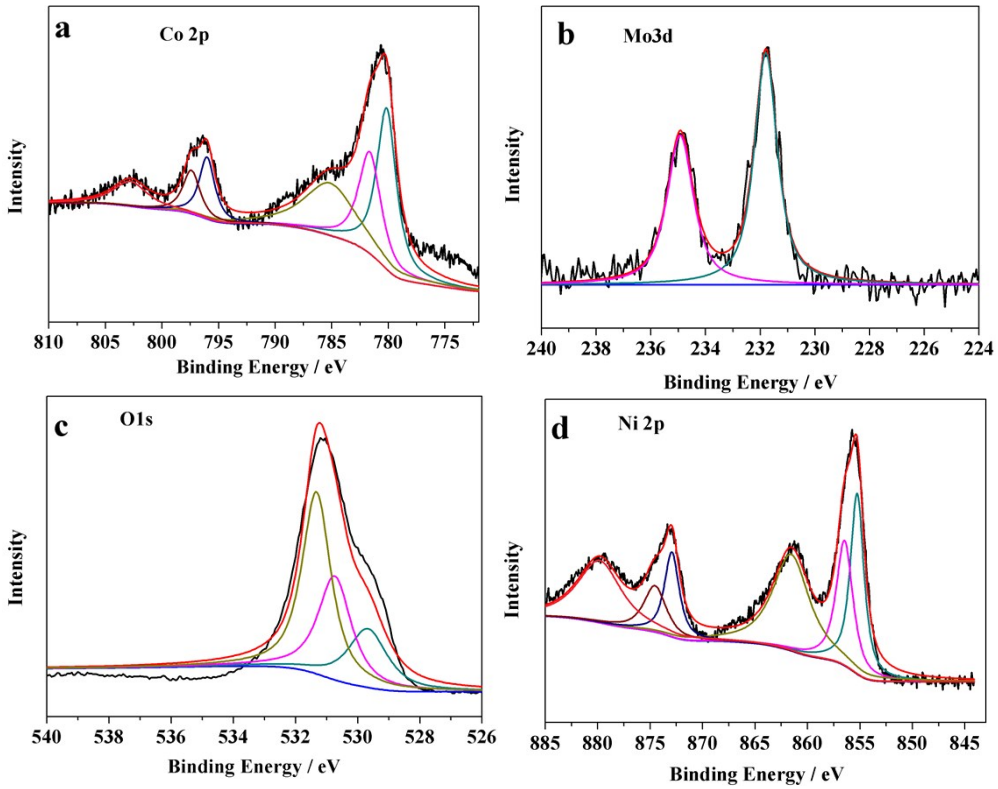

Fig.S6 XPS of (a) Co 2p, (b) Mo 3d, (c) O 1s and (d) Ni 2p of $CoMoO_4$@$CoNiO_2/O_2$.

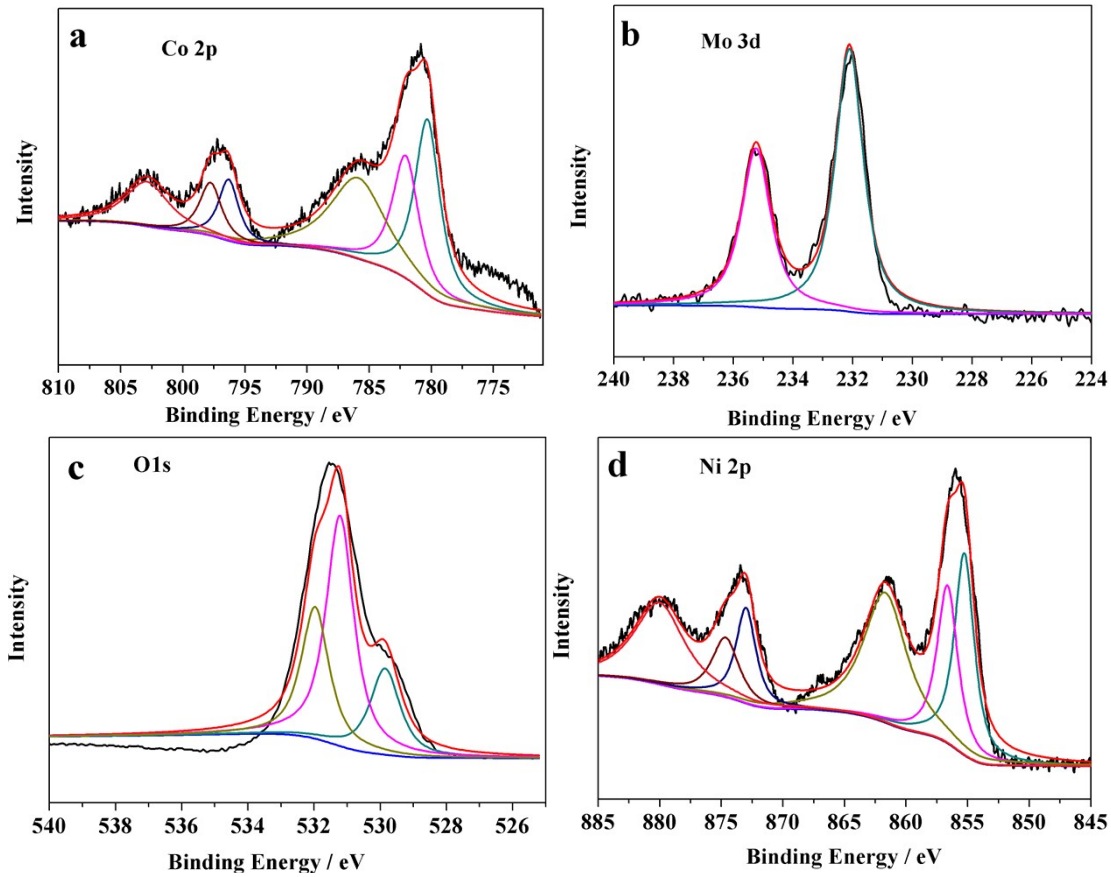

Fig.S7 XPS of (a) Co 2p, (b) Mo 3d, (c) O 1s and (d) Ni 2p of $CoMoO_4$@$CoNiO_2$/Ar.

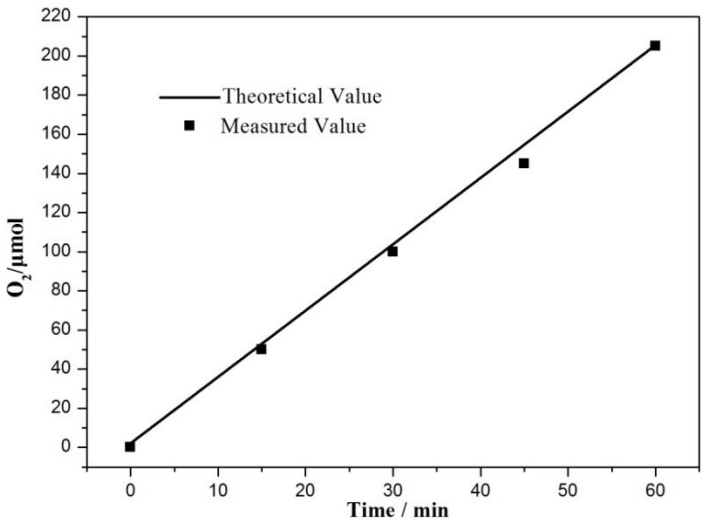

Fig. S8 Electrocatalytic efficiency of O_2 production over $CoMoO_4$@$CoNiO_2$/Ar at a potential of ca. 1.50 V, measured for 60 min.

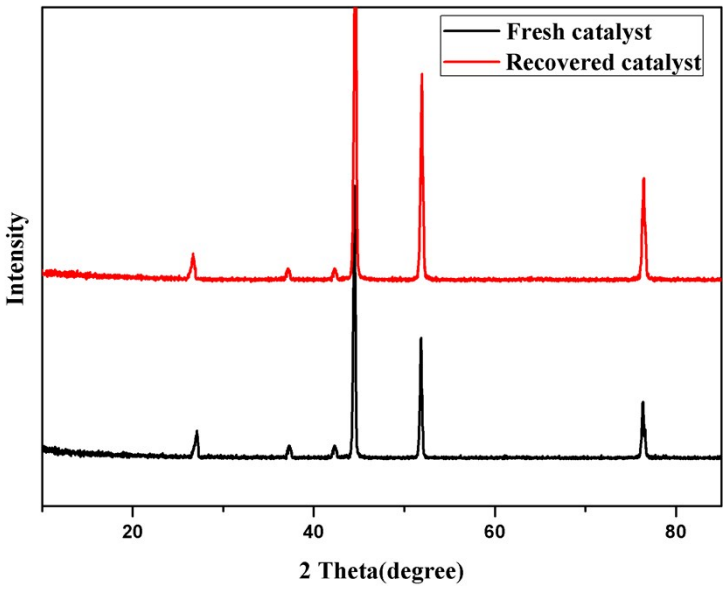

Fig.S9 XRD of fresh (a) and recovered (b) $CoMoO_4$@$CoNiO_2$/Ar.

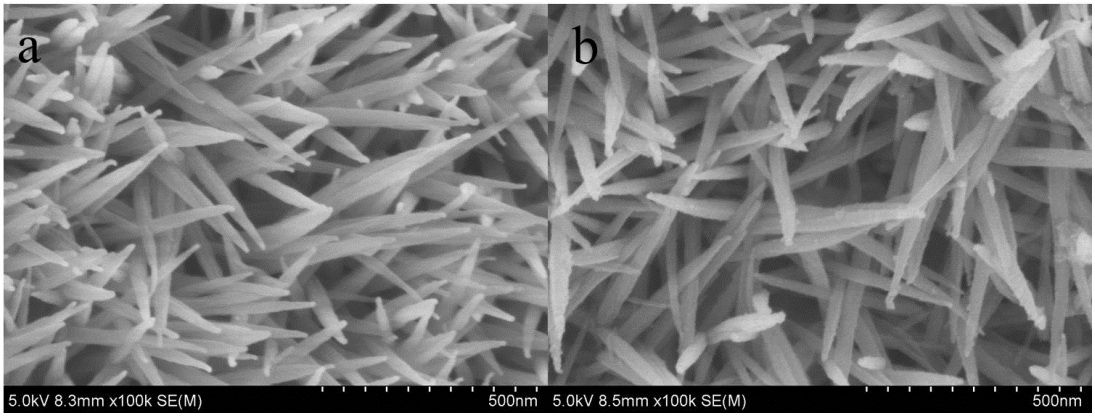

Fig.S10 SEM of fresh (a) and recovered (b) $CoMoO_4$@$CoNiO_2$/Ar.

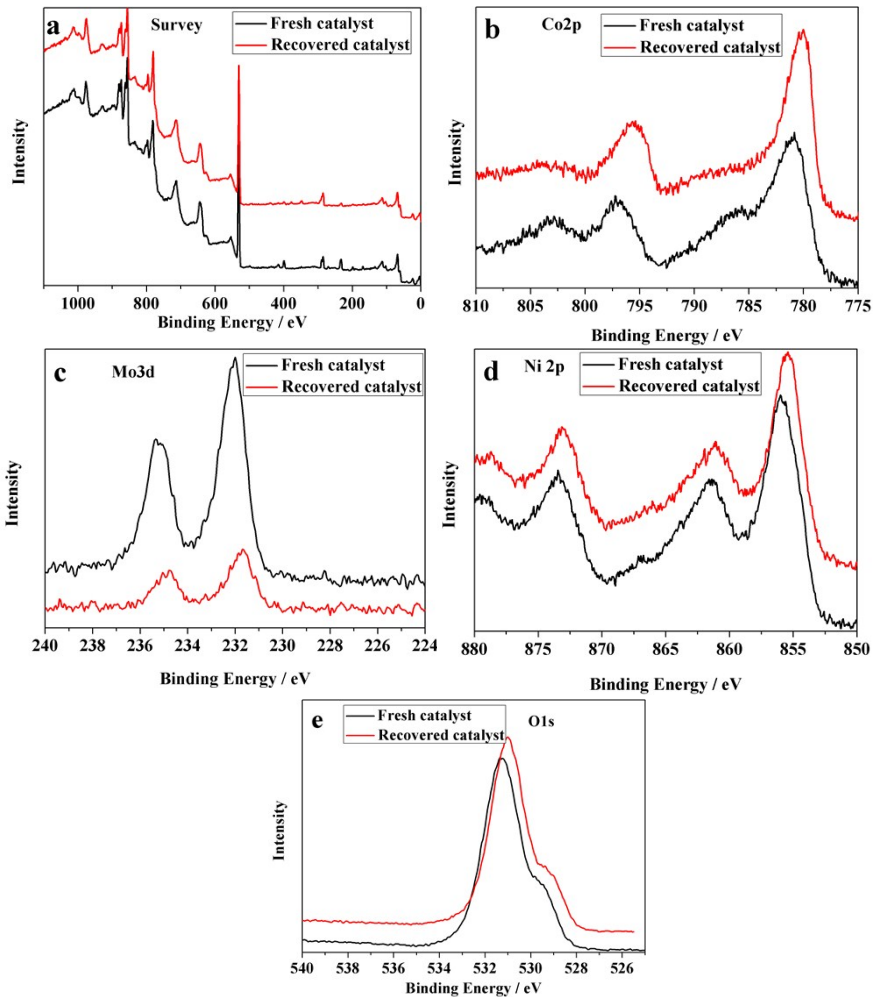

Fig.S11 XPS of (a) survey scan, (b) Co 2p, (c) Mo 3d, (d) Ni 2p and (e) O 1s of fresh and recovered $CoMoO_4$@$CoNiO_2$/Ar.

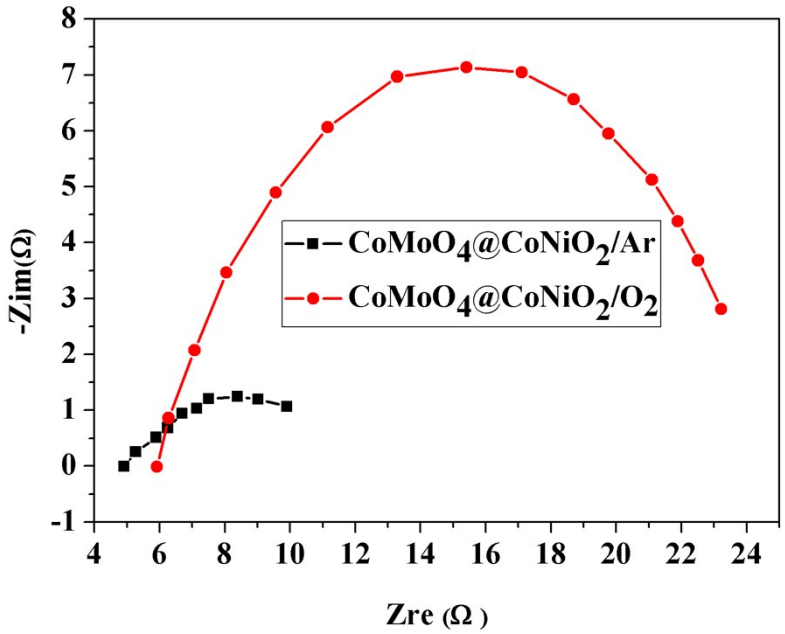

Fig.S12 Nyquist plots of samples.

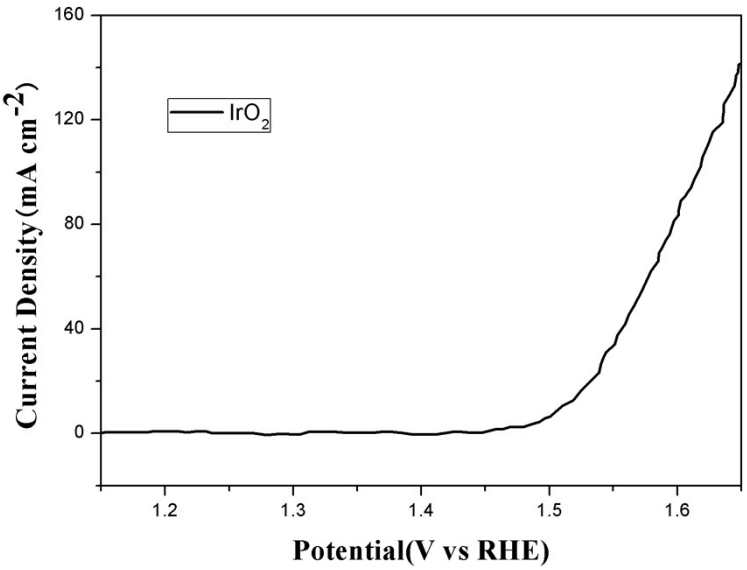

Fig. S13 OER curves of IrO_2 in 1.0 M KOH.

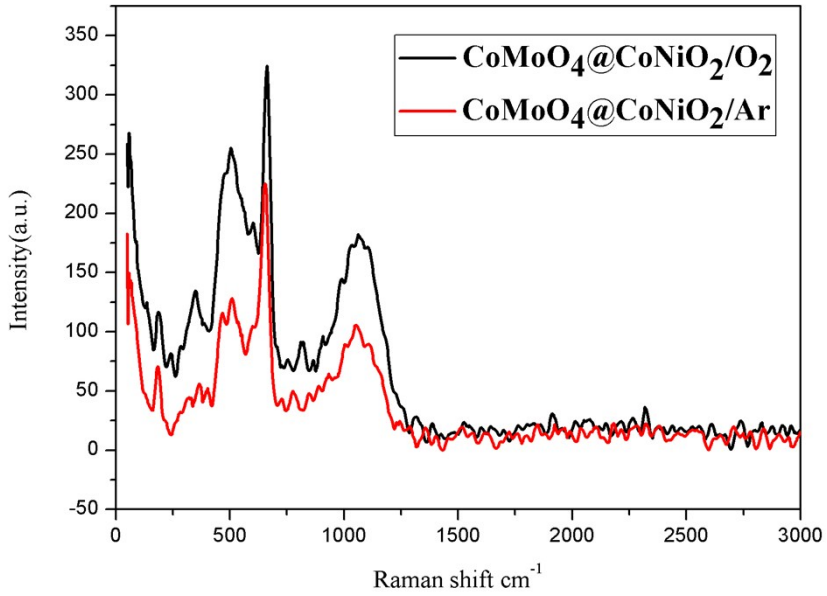

Figure S14. Raman spectrum of $CoMoO_4$@$CoNiO_2$ excited by 514.5 nm laser.

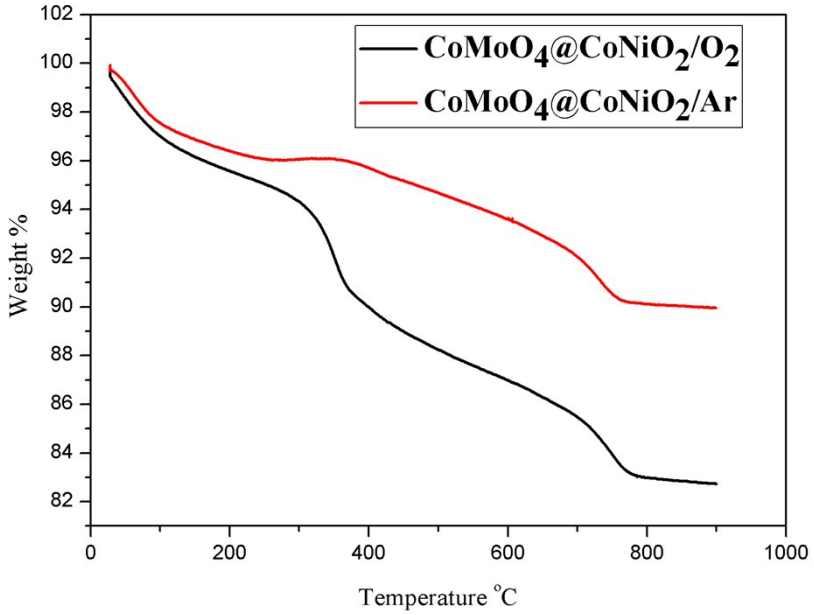

Figure S15. Thermograrimetric analysis of $CoMoO_4$@$CoNiO_2$/O_2 and $CoMoO_4$@$CoNiO_2$/Ar.

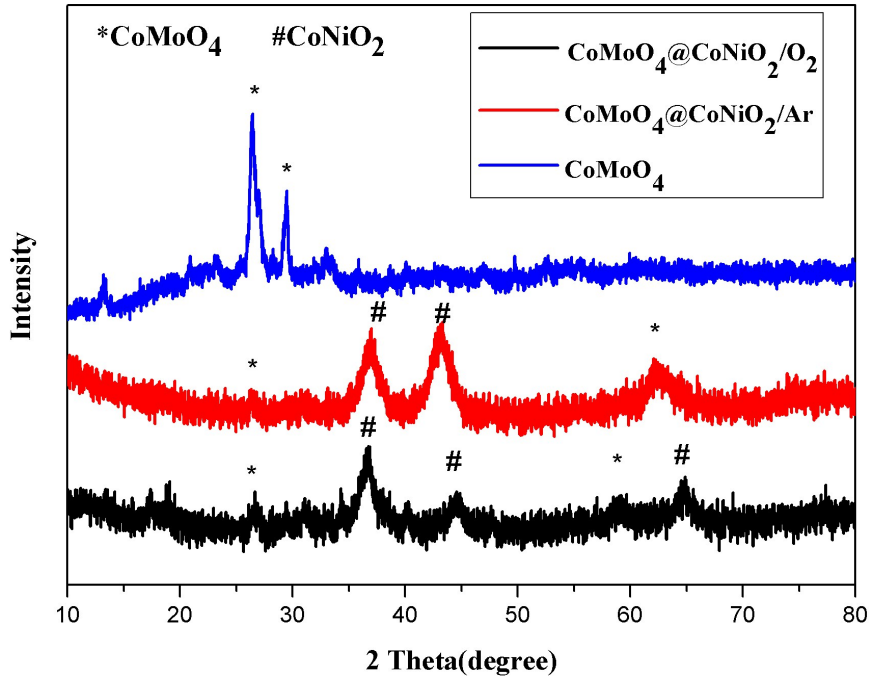

Fig. S16 XRD of $CoMoO_4$, $CoMoO_4$@$CoNiO_2$/O_2 and $CoMoO_4$@$CoNiO_2$/Ar. (The oxides have been physically separated from the support)